Frontiers of Information Technology & Electronic Engineering
www.jzus.zju.edu.cn; engineering.cae.cn; www.springerlink.com
ISSN 2095-9184 (print); ISSN 2095-9230 (online)
E-mail: jzus@zju.edu.cn

A low-profile dual-broadband dual-circularly-polarized reflectarray for K-/Ka-band space applications*

Xuanfeng TONG[1], Zhi Hao JIANG[†‡1,2], Yuan LI[1], Fan WU[1], Lin PENG[3], Taiwei YUE[4], Wei HONG[1,2]
[1]State Key Laboratory of Millimeter Waves, School of Information Science and Engineering, Southeast University, Nanjing 210096, China
[2]Purple Mountain Laboratories, Nanjing 211111, China
[3]State Key Laboratory of Mobile Network and Mobile Multimedia Technology, ZTE Corporation, Shenzhen 518057, China
[4]Apple Inc., One Apple Park Way, Cupertino, CA 95014, USA
[†]E-mail: zhihao.jiang@seu.edu.cn

Received Mar. 28, 2023; Revision accepted Sept. 18, 2023; Crosschecked July 31, 2024

Abstract: A low-profile dual-broadband dual-circularly-polarized (dual-CP) reflectarray (RA) is proposed and demonstrated, supporting independent beamforming for right-/left-handed CP waves at both K-band and Ka-band. Such functionality is achieved by incorporating multi-layered phase shifting elements individually operating in the K- and Ka-band, which are then interleaved in a shared aperture, resulting in a cell thickness of only about $0.1\lambda_{\mathrm{L}}$. By rotating the designed K- and Ka-band elements around their own geometrical centers, the dual-CP waves in each band can be modulated separately. To reduce the overall profile, planar K-/Ka-band dual-CP feeds with a broad band are designed based on the magnetoelectric dipoles and multi-branch hybrid couplers. The planar feeds achieve bandwidths of about 32% and 26% at K- and Ka-band respectively with reflection magnitudes below −13 dB, an axial ratio smaller than 2 dB, and a gain variation of less than 1 dB. A proof-of-concept dual-band dual-CP RA integrated with the planar feeds is fabricated and characterized which is capable of generating asymmetrically distributed dual-band dual-CP beams. The measured peak gain values of the beams are around 24.3 and 27.3 dBic, with joint gain variation <1 dB and axial ratio <2 dB bandwidths wider than 20.6% and 14.6% at the lower and higher bands, respectively. The demonstrated dual-broadband dual-CP RA with four degrees of freedom of beamforming could be a promising candidate for space and satellite communications.

Key words: Broadband; Dual-band; Dual-circularly-polarized; Reflectarray; Shared-aperture
https://doi.org/10.1631/FITEE.2300214 **CLC number:** TN82

1 Introduction

Due to the fast-growing demands of commercial wireless communications for a higher speed of data transmission and a better coverage of the Earth's surface, existing ground-based communication infrastructures can no longer satisfy future needs. Looking to the future, a three-dimensional (3D) network merging base stations on the ground and satellites in low and medium Earth orbits (LEO and MEO), as well as those in the geostationary orbit (GEO), can enable a universal wireless coverage of the entire surface of the Earth with a high-speed connection (Hong et al., 2021; Amendola et al., 2023; Sheng et al., 2023). One of the technologies enabling such a network is high throughput satellite (HTS) communications (Fenech et al., 2015; Fenech, 2021), in which multiple beams are generated to cover a certain area of the Earth, with each beam pointing to a specific region (Martinez-de-Rioja E et al., 2019). Typically, a four-color scheme is

---

‡ Corresponding author

* Project supported by the National Natural Science Foundation of China (Nos. 62122019, 62293492, and 61901106), the ZTE Corporation and the State Key Laboratory of Mobile Network and Mobile Multimedia Technology, and the Fundamental Research Funds for Central Universities, China (No. 2242022k60008)

ORCID: Xuanfeng TONG, https://orcid.org/0000-0001-8730-9331; Zhi Hao JIANG, https://orcid.org/0000-0002-4275-1203

employed such that the adjacent beams either belong to different operational frequency bands or have orthogonal circular polarizations for uploading and downloading data (Zhou et al., 2020; Martinez-de-Rioja D et al., 2021), thereby suppressing inter-beam interference. To this end, radiating apertures that can provide dual-band dual-circularly-polarized (CP) beamforming are highly desirable, and can be realized by using antenna arrays (Garcia-Aguilar et al., 2012; Luo et al., 2016; Wu et al., 2018; Zhao and Luk, 2018; Mao et al., 2019) and reflectarrays/transmitarrays (RAs/TAs) (Luo et al., 2019; Naseri et al., 2020; Xu et al., 2021; Tong et al., 2022). Compared to antenna arrays and TAs, RAs possess advantages such as ease of design and implementation, high efficiency, low cost, being lightweight, and/or low power distributing loss. This makes them ideal candidates, particularly for space applications (Huang and Encinar, 2008). Hence, RAs with dual-band and/or dual-CP beamforming capabilities have garnered a tremendous amount of research interest (Cheng and Abbaspour-Tamijani, 2009; Nayeri et al., 2015).

Over the past decade, investigations and designs of RAs supporting either dual-band or dual-CP operation have been reported. Dual-band RAs can be synthesized using three approaches. The first one uses dual-band multi-resonance RA cells that can provide controllable reflective phase shifts at both prescribed operational frequency bands for either linear or circular polarization (Malfajani and Atlasbaf, 2014; Deng et al., 2017a, 2017b). The second method achieves dual-band beamforming by aligning two types of reflective phasing elements, which are active at either the lower or higher band, in an interleaved manner (Smith et al., 2013; Shamsaee Malfajani and Abbasi Arand, 2017; Su et al., 2019). The third approach places the phase shifting cells responsible for the lower- and higher-band on different layers, which are separated by a frequency selective surface (FSS) to suppress inter-band coupling (Chaharmir and Shaker, 2015; Deng et al., 2017c, 2018). On the other hand, dual-CP RAs with independent control of polarization have also been studied; they can enhance spectral efficiency and are classified into three categories. The first kind relies on dual-functional-layer structures, each offering rotation phase compensation of CP waves with a distinct handedness (Mener et al., 2014, 2015; Li Y et al., 2022). The second type of dual-CP RA is enabled by placing a circular polarizer on top of a dual-linearly-polarized (dual-LP) RA (Joyal et al., 2015; Geaney et al., 2019). By jointly exploiting the dynamic and rotation phases, the last method requires only a single functional layer (Florencio et al., 2019; Guo et al., 2020; Jiang et al., 2020a, 2020b; Zhang et al., 2021), which can be realized by dual-LP RA cells with pre-designed geometrical rotation angles.

Recently, advanced RAs with simultaneous dual-band and dual-CP characteristics are becoming increasingly attractive. Their four degrees of freedom of beamforming in a shared-aperture configuration can potentially facilitate the reduction of the number of radiating apertures on satellites for four-color multi-beam coverage (Martinez-de-Rioja E et al., 2019). However, only a few RA designs of this kind have been reported (Luo et al., 2019; Naseri et al., 2020; Xu et al., 2021; Tong et al., 2022). In Naseri et al. (2020) and Xu et al. (2021), dual-band dual-CP RAs based on multiple functional layers were demonstrated. The former, with a total panel thickness of $1.23\lambda_{\mathrm{L}}$ (λ_{L} is the free-space wavelength at the lower band), used a dual-band circular polarizer on top and a dual-band dual-LP RA on the bottom, achieving 1-dB gain bandwidths of less than 3% at both the K- and Ka-band (Naseri et al., 2020). The latter, with a total panel thickness of $0.52\lambda_{\mathrm{L}}$, employed Ku- and Ka-band cross-dipole elements on the top and bottom, which were separated by an FSS, offering joint 1-dB gain and 3-dB axial ratio (AR) bandwidths of less than 5% (Xu et al., 2021). In Luo et al. (2019), two triangular patches, fed by hybrid couplers with open-circuit delay line loadings, were incorporated in each RA cell to enable dual-band dual-CP beamforming at 8.6 and 10 GHz. Although there was only a single functional layer with a panel thickness of $0.02\lambda_{\mathrm{L}}$, the operational bandwidths were smaller than 4%, with the beam radiating angles being limited by the large cell size of $0.64\lambda_{\mathrm{L}}$. More recently, by properly exploiting the interleaving element alignment strategy and jointly using dynamic and rotation phases, a shared-aperture dual-band dual-CP RA based on dual-LP aperture-coupled patches loaded with shorted delay lines has been realized (Tong et al., 2022). It possessed a panel thickness of $0.27\lambda_{\mathrm{L}}$ and offered joint 1-dB gain and AR<2 dB bandwidths of 7.3% and 6.7% at the K- and Ka-band, respectively. Although these designs are capable of providing dual-band dual-CP beamforming, their operational bands are too narrow to be useful in practical applications.

In this paper, we present the design and experimental validation of a shared-aperture dual-broadband dual-CP RA with four degrees of freedom, which possesses a panel thickness of only $0.1\lambda_{\rm L}$, by using cascaded phase shifting surfaces. Instead of horn antennas, broadband dual-CP feeds are designed for illuminating the RA, enabling a small focal-to-diameter (F/D) ratio of 0.6, which can reduce the overall profile of the integrated RA antenna. A proof-of-concept RA is fabricated and measured, achieving greatly enhanced joint 1-dB gain and AR<2 dB bandwidths of more than 20.6% and 14.6% at K- and Ka-band, respectively, representing a new state of the art for dual-band dual-CP RAs.

2 Design of RA unit cells for dual-band dual-CP phase compensation

The configuration of the proposed dual-band dual-CP RA (Fig. 1a) has a quasi-circular aperture. Different from using horn antennas as seen in most RA/TA designs (Huang and Encinar, 2008), here planar feeds are employed which can reduce the overall profile of the final antenna module. To truly achieve dual-band dual-CP radiation, two dual-CP feed radiators, operating at K- and Ka-band, separately, are used. For each feed, it has two input ports for generating broadband and symmetrical left-handed CP (LCP) and right-handed CP (RCP) beams such that the dual-band dual-CP beams can be individually excited without changing the feeds (Jiang et al., 2021). Correspondingly, the RA is composed of cells containing interleaved elements (labeled with yellow and green colors) that are responsible for providing independent dual-CP reflective phase compensation at K- and Ka-band, respectively, i.e., $\phi_{\rm L,K}$, $\phi_{\rm L,Ka}$, $\phi_{\rm R,K}$, and $\phi_{\rm R,Ka}$, with a high efficiency. When the LCP ports of the two feeds are excited, a directive LCP beam can be generated which points at a deflected angle of $(\theta_{\rm L}, \varphi_{\rm L})_{\rm K}$ and $(\theta_{\rm L}, \varphi_{\rm L})_{\rm Ka}$ at the K- and Ka-band, respectively. On the other hand, the RA antenna can generate RCP beams pointing at an oblique angle of $(\theta_{\rm R}, \varphi_{\rm R})_{\rm K}$ and $(\theta_{\rm R}, \varphi_{\rm R})_{\rm Ka}$ away from the RA normal at the K- and Ka-band, respectively, when the RCP ports

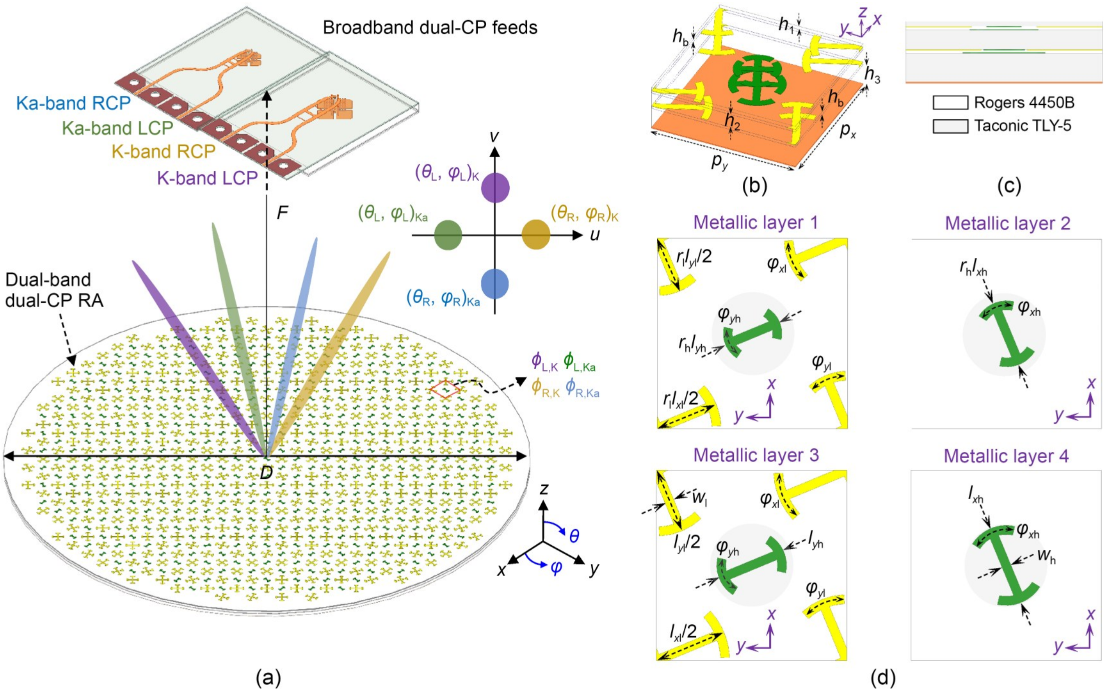

Fig. 1 (a) Configuration of the dual-band dual-CP RA antenna generating K- and Ka-band RCP and LCP beams pointing at different angles when excited by K- and Ka-band dual-CP planar feeds; (b) 3D view of the dual-band dual-CP RA cell; (c) side view of the dual-band dual-CP RA cell; (d) planar views of the metallic layers. The geometrical dimensions are p_x=5 mm, p_y=5 mm, h_1=0.13 mm, h_2=0.51 mm, h_3=0.76 mm, $h_{\rm b}$=0.1 mm, $\varphi_{x\rm l}$=20°, $\varphi_{x\rm h}$=35°, $\varphi_{y\rm l}$=20°, $\varphi_{y\rm h}$=35°, $w_{\rm l}$=0.25 mm, $w_{\rm h}$=0.25 mm. References to color refer to the online version of this figure

of the two feeds are active. In the remainder of this section, the derivation of the reflection coefficient matrix and the evolution of the dual-band dual-CP RA cell designs are presented, followed by the simulated properties of the RA cells at oblique incident angles.

2.1 Derivation of the reflection coefficient matrix

The reflection coefficient matrix, which can explain the relationships between the incident and reflected wave vectors, has been widely employed to characterize the scattering properties of periodic structures. The reflection coefficient matrix of an RA cell can be written either on the linear polarization basis ($\boldsymbol{S}_{\text{lin}}=[r_{xx}, r_{xy}; r_{yx}, r_{yy}]$) or on the circular polarization basis ($\boldsymbol{S}_{\text{cir}}=[r_{\text{RR}}, r_{\text{RL}}; r_{\text{LR}}, r_{\text{LL}}]$). They can be interchanged as

$$\begin{cases} r_{\text{RR}} = 0.5(r_{xx} - r_{yy} + \text{j}r_{xy} + \text{j}r_{yx})\text{e}^{\text{j}2\phi_{\text{r}}}, \\ r_{\text{RL}} = 0.5(r_{xx} + r_{yy} - \text{j}r_{xy} + \text{j}r_{yx}), \\ r_{\text{LR}} = 0.5(r_{xx} + r_{yy} + \text{j}r_{xy} - \text{j}r_{yx}), \\ r_{\text{LL}} = 0.5(r_{xx} - r_{yy} - \text{j}r_{xy} - \text{j}r_{yx})\text{e}^{-\text{j}2\phi_{\text{r}}}, \end{cases} \tag{1}$$

$$\begin{cases} r_{xx} = 0.5(r_{\text{RR}}\text{e}^{-\text{j}2\phi_{\text{r}}} + r_{\text{LL}}\text{e}^{\text{j}2\phi_{\text{r}}} + \text{j}r_{\text{RL}} + \text{j}r_{\text{LR}}), \\ r_{xy} = 0.5(r_{\text{RR}}\text{e}^{-\text{j}2\phi_{\text{r}}} - r_{\text{LL}}\text{e}^{\text{j}2\phi_{\text{r}}} - \text{j}r_{\text{RL}} + \text{j}r_{\text{LR}}), \\ r_{yx} = 0.5(r_{\text{RR}}\text{e}^{-\text{j}2\phi_{\text{r}}} - r_{\text{LL}}\text{e}^{\text{j}2\phi_{\text{r}}} + \text{j}r_{\text{RL}} - \text{j}r_{\text{LR}}), \\ r_{yy} = 0.5(r_{\text{RR}}\text{e}^{-\text{j}2\phi_{\text{r}}} + r_{\text{LL}}\text{e}^{\text{j}2\phi_{\text{r}}} - \text{j}r_{\text{RL}} - \text{j}r_{\text{LR}}), \end{cases} \tag{2}$$

where ϕ_{r} is the in-plane rotation angle of the RA cell.

For a true dual-CP RA cell, for example, the co-polarized CP magnitudes should be near unity, while it should be possible to independently control the co-polarized CP phases. Meanwhile, the cross-polarized CP magnitudes need to be zero for ensuring high CP purity, hence assuming that the reflection coefficient matrix in the circular polarization basis can be written as

$$\boldsymbol{S}_{\text{cir}} = \begin{bmatrix} \text{e}^{\text{j}\phi_{\text{RR}}} & 0 \\ 0 & \text{e}^{\text{j}\phi_{\text{LL}}} \end{bmatrix}. \tag{3}$$

The reflection coefficient matrix in the linear polarization basis can then be obtained by substituting Eq. (3) into Eq. (2) as

$$\boldsymbol{S}_{\text{lin}} = \text{e}^{\text{j}\phi_{\text{n}}} \begin{bmatrix} 1 & 0 \\ 0 & -1 \end{bmatrix}, \tag{4}$$

under the condition that the cross-polarized LP magnitudes are assumed to be zero, where $\phi_{\text{n}}=\phi_{\text{RR}}-2\phi_{\text{r}}=\phi_{\text{LL}}+2\phi_{\text{r}}$ is the dynamic phase of RA cells. It can be concluded from Eq. (4) that co-polarized CP phases can be controlled separately by modifying the dynamic phase (ϕ_{n}) and in-plane rotation angle (ϕ_{r}) of RA cells.

In the above derivation, the co-polarized LP/CP magnitudes are assumed to be unity, while, accordingly, the cross-polarized LP/CP magnitudes are assumed to be zero. However, it is impossible for an RA cell to possess such perfect properties. As a result, it is important to theoretically analyze the influence of the non-zero cross polarization reflection and imperfect phase difference between the two optical axes on the dual-CP reflection properties of the RA cell. Specifically, the reflection coefficient matrix of the RA cell can be written in a generalized form as

$$\boldsymbol{S}_{\text{lin}} = \begin{bmatrix} |r_{xx}|\text{e}^{\text{j}\phi_{xx}} & |r_{xy}|\text{e}^{\text{j}\phi_{xy}} \\ |r_{yx}|\text{e}^{\text{j}\phi_{yx}} & |r_{yy}|\text{e}^{\text{j}\phi_{yy}} \end{bmatrix}, \tag{5}$$

where

$$|r_{xx}|^2 + |r_{yx}|^2 = 1, \tag{6a}$$

$$|r_{xy}|^2 + |r_{yy}|^2 = 1, \tag{6b}$$

$$|r_{xy}| = |r_{yx}|, \tag{6c}$$

$$\phi_{xy} = \phi_{yx}, \tag{6d}$$

$$2\phi_{xy} = \phi_{xx} + \phi_{yy} + (2n+1)\pi, n = 0, 1, 2, \cdots, \tag{6e}$$

for satisfying the lossless, energy conservation, and time-reversal symmetry conditions (Wang DY et al., 2021). By substituting Eq. (5) into Eq. (1), the relationships of co-polarized CP reflection efficiency and AR as a function of the co-polarized LP magnitudes and phase difference are obtained (Fig. 2). It can be seen that, when the co-polarized LP reflection coefficients have a magnitude higher than 0.6 and a phase difference within 180°±19.2°, the AR values can be maintained below 3 dB with a CP reflection efficiency higher than 97.2%.

2.2 RA cell structure

The 3D configuration of the dual-band dual-CP RA cell (Fig. 1b) has a unit cell size of 5 mm×5 mm, i.e., about $(\lambda_0/2)\times(\lambda_0/2)$ at the higher frequency Ka-band of 30 GHz. The structure comprises multi-layered phase shifting surfaces (Gagnon et al., 2013) consisting of subwavelength metallic resonators and a ground plane separated by dielectric substrates, altogether including five metallic layers. As shown from the side view of the unit cell (Fig. 1c), three layers of Taconic TLY-5 substrates (ε_r=2.2, δ_{tan}=0.0009) are employed with thicknesses of h_1=0.13 mm, h_2=0.51 mm, and h_3=0.76 mm, separately, which are bonded by two Rogers 4450B (ε_r=3.54, δ_{tan}=0.0014) films with a thickness of h_b=0.1 mm. Thus, the total thickness of the structure is 1.6 mm, i.e., about $0.1\lambda_L$ at 19 GHz.

The cell contains elements operating at the lower and higher frequency bands, respectively, which are denoted as the K-band element (in yellow) and the Ka-band element (in green). Planar views of the metallic patterns on different layers are displayed in Fig. 1d. The K-band element contains two cascaded connected crossed-dipoles printed on the bottom sides of the first and second TLY-5 substrate layers. The lengths of the upper crossed-dipoles have a scaling factor of r_l as compared to the lower ones. On the other hand, the Ka-band element contains crossed-dipoles that are not interconnected to avoid in-band spurious resonant modes that could occur at oblique incidence (Liu et al., 2017). Half of the dipoles are located on the bottom sides of the first and second TLY-5 substrate layers, while the two other orthogonally-oriented dipoles are placed on the top surfaces of the second and third TLY-5 substrate layers. The lengths of the two upper dipoles are scaled by a factor of r_h as compared to the lower ones.

To achieve independent dual-CP phase shifting at both K-band and Ka-band, four degrees of freedom are required. This can be provided by the joint dynamic and rotation phase strategy (Jiang et al., 2020a), implying that the cells should possess the following electrical properties simultaneously at both bands. First, they should behave like a reflective half-wave plate that transforms the RCP or LCP incident wave into the same CP reflected wave with a near-unity reflectivity. Second, they should be able to provide a dynamic phase coverage of a full 360° by changing the geometrical dimensions of the dipole resonators, which can be used to introduce the same amount of phase shifts for the RCP and LCP waves. Third, all the elements can be rotated around their own geometrical centers by certain angles, i.e., ϕ_{rl} and ϕ_{rh}, to offer the desirable rotation phases that can impose opposite phase compensation for the RCP and LCP waves and thereby distinguish between them. Consequently, the K- and Ka-band elements need to be confined within different circular areas (labeled as grey and pale blue in Fig. 1d) with the largest possible distance in between for reducing inter-element coupling, which could possibly induce phase errors as the elements rotate (Tong et al., 2022). This requires that all the dipole resonators should be miniaturized to a certain extent. Consequently, arc-shaped end loadings are added on the dipole resonators of all the elements (Selvanayagam and Eleftheriades, 2016).

2.3 Design evolution of RA cells

When designing the RA cells with independent dual-band dual-CP phase compensation, the mutual impacts of the elements operating separately at K- and Ka-band need to be considered. Since the resonators operating at the higher frequency band have a smaller size and a weaker dipole moment than those designed to function at the lower frequency band, their impact

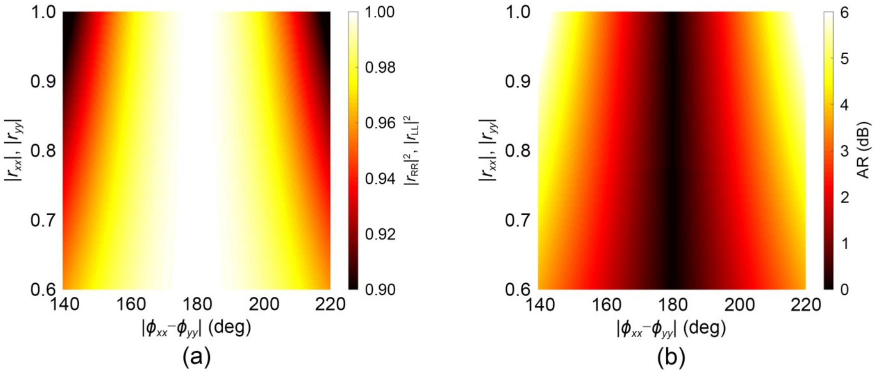

Fig. 2 The calculated co-polarized CP reflection efficiency (a) and AR (b) as a function of the co-polarized LP magnitudes and phase difference

on the K-band elements is typically very small and can even be neglected in engineering designs (Sofi et al., 2020). Due to this fact, the design evolution of the RA cell undergoes three steps, starting from RA cell A for the K-band dual-LP operation to RA cell B for the dual-band dual-LP operation, and finally to RA cell C for the targeted dual-band dual-CP operation (Fig. 3). High Frequency Structure Simulator (HFSS) based on a full-wave finite element method is used to predict the scattering properties of the RA cells, where periodic boundary conditions are assigned to the lateral walls and a Floquet port is placed on the top for dual-polarized plane-wave excitation (Wang YF et al., 2022).

In the first step, for RA cell A, as shown in Fig. 3a, only the K-band elements containing dual-layered crossed-dipoles are considered. Such a dual-layer structure can provide a second-order response, whose transfer function is governed by the resonances of each layer and the coupling between them. For RA cells, the reflective phase linearity is an important property that determines the operational bandwidth of the final array, which can be controlled by the size scaling parameter r_l (Encinar and Zornoza, 2003). As shown in Figs. 4a–4c, by varying the length of the dipoles along the x-direction from $l_{x\mathrm{l}}$=3.1 to 3.9 mm with r_l=0.75, 0.85, and 0.95, it can be seen that the simulated $\phi(r_{xx})$, at normal incidence, undergoes a monotonic reduction at all three frequencies of 18, 19, and 20 GHz. When r_l=0.75, $\phi(r_{xx})$ can cover a phase range of only about 270° at K-band, which is not enough to provide a full-period coverage. For the case of r_l=0.95, the phase coverage is greatly increased to more than 500°; however, a poor phase linearity is exhibited due to the increased quality factor. In this situation, a region with more abrupt phase variation can be identified when $l_{x\mathrm{l}}$ is around 3.3, 3.5, and 3.7 mm at 18, 19, and 20 GHz, respectively. When a proper value of r_l=0.85 is selected, the phase curves at all three frequencies are nearly parallel to each other and exhibit a good linearity versus $l_{x\mathrm{l}}$. In addition, to investigate the potential impact of the K-band elements on the reflection phase in the Ka-band, plots of the simulated $\phi(r_{xx})$ as a function of $l_{x\mathrm{l}}$ at 30, 31, and 32 GHz are shown. It can be observed that, as the value of r_l increases, $\phi(r_{xx})$ becomes more stable as a function of $l_{x\mathrm{l}}$, e.g., $\Delta\phi(r_{xx})$ ≤40° when r_l=0.85, implying a smaller cross-band coupling. This is attributed to the increased quality factor and the resulting sharper filtering response of the second-order transfer function of the element. The cross-polarization coupling can be evaluated by observing the variation of the simulated

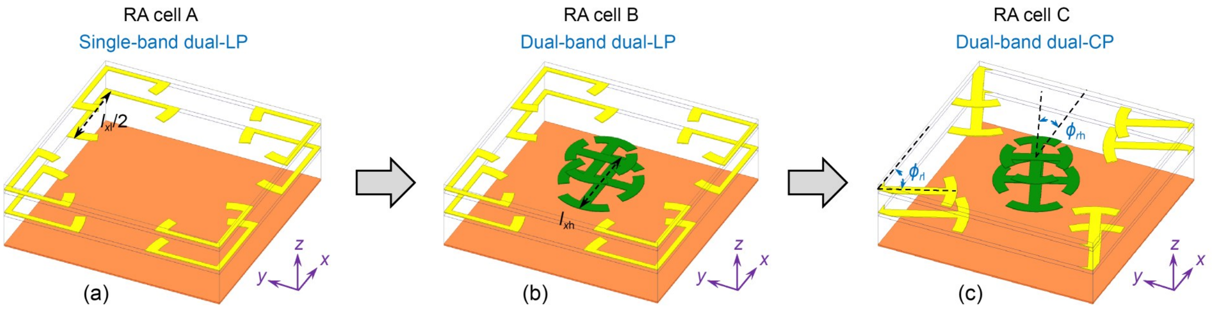

Fig. 3 Evolution of the RA cell designs from RA cell A (a) to RA cell B (b) and finally to RA cell C (c)

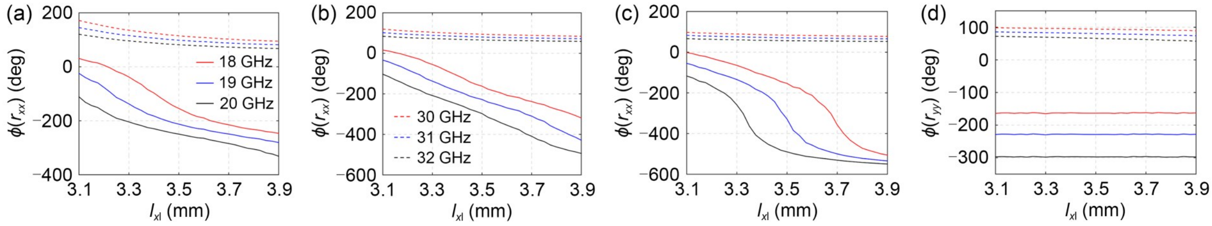

Fig. 4 Simulated $\phi(r_{xx})$ of RA cell A for r_l=0.75 (a), r_l=0.85 (b), and r_l=0.95 (c), as well as simulated $\phi(r_{yy})$ of RA cell A (d) at K-band (18, 19, and 20 GHz, as shown by solid lines) and Ka-band (30, 31, and 32 GHz, as shown by dashed lines) as a function of $l_{x\mathrm{l}}$. References to color refer to the online version of this figure

$\phi(r_{yy})$ as a function of $l_{x\mathrm{l}}$, as shown in Fig. 4d. Due to the inherent mirror symmetry of the structure, the variation of $\phi(r_{yy})$ is smaller than 5° and 15° in the K- and Ka-band, respectively, indicating that cross-polarization coupling is negligible at both bands. It should be noted that, for all these cases, the reflection magnitude (R_{xx}) is above −0.3 dB, which is not shown here for succinctness.

Based on the designed RA cell A, in the second step, Ka-band elements are further introduced into the cell to enable dual-band dual-LP phase shifting by adding the dual-layered crossed-dipoles that are not interconnected (Fig. 3b). At normal incidence, the simulated $\phi(r_{xx})$ as a function of $l_{x\mathrm{h}}$, the length of the Ka-band crossed-dipoles along the x-direction, at three frequencies of 30, 31, and 32 GHz, are reported in Figs. 5a–5c, with r_h=0.7, 0.8, and 0.9. Similar to the phenomenon observed in RA cell A, for RA cell B, those with a smaller r_h can provide only a limited phase coverage of less than 200°, while the designs with a larger r_h suffer from a poor phase linearity. When r_h=0.8, all three phase curves possess a good linearity, which would give rise to a wideband response. In contrast to the K-band elements, the Ka-band elements have a very minor impact on the reflective phase at the lower frequency band, as it can be seen that $\Delta\phi(r_{xx})$ is on average smaller than 10°, which is irrelevant to the choice of r_h. Regarding cross-polarization coupling, similarly, $\Delta\phi(r_{yy})$ experiences a very small variation of less than 5° when $l_{x\mathrm{h}}$ is changed. Note that these Ka-band elements need to be designed with the presence of the K-band elements. This is because, although the lower-band elements with different values of $l_{x\mathrm{l}}$ have similar electromagnetic responses at the Ka-band, they have a certain number of non-negligible dipole moments and thus should be taken into account during the design of the higher-band elements (Smith et al., 2013).

Once the investigation of RA cell B is complete, a library of constitutive cells can be formed by selecting proper values of $l_{x\mathrm{l}}$ and $l_{x\mathrm{h}}$ such that they provide independent dynamic phase shifting for both the K- and Ka-band, which can fulfill the second requirement stated in Section 2.2. Here, a 3×3-bit dynamic phase resolution, i.e., the reflection phases of both $\phi(r_{xx})$ and $\phi(r_{yy})$ having a 3-bit resolution, is targeted for the two linear polarizations, and can be used to synthesize 2×2-bit dual-CP phase compensation at both bands. It has been shown that the 2-bit strategy is a good trade-off between the phase-error-induced gain loss and design complexity (Abdelrahman et al., 2017). To this end, 16 designs of RA cell B are selected with $l_{x\mathrm{l}}$=3.9, 3.8, 3.7, and 3.6 mm and $l_{x\mathrm{h}}$=2.27, 2.21, 2.15, and 2.09 mm. They are designated as Cell_{mn} with m=1, 2, 3, 4 and n=1, 2, 3, 4, which are composed of four K-band elements denoted as $\mathrm{Ele}_{\mathrm{L}m}$ and four Ka-band elements denoted as $\mathrm{Ele}_{\mathrm{H}n}$. In addition, for all the 16 cells, the dipoles oriented along the x- and y-direction possess different length values where $l_{y\mathrm{l}}$ and $l_{y\mathrm{h}}$ are selected to be $l_{y\mathrm{l}}=l_{x\mathrm{l}}-0.4$ mm and $l_{y\mathrm{h}}=l_{x\mathrm{h}}-0.28$ mm, ensuring that $\phi(r_{xx})$ and $\phi(r_{yy})$ have a phase difference of around 180°.

The CP reflection coefficients of the library of 16 cell designs, transformed from the LP reflection coefficients (Sanz-Fernández et al., 2015), are shown in Fig. 6 for both the K-band and Ka-band. It can be seen that, at the lower band from 17 to 21 GHz, the co-polarized CP reflection magnitudes, i.e., R_LL and R_RR, are higher than −1 dB for most of the cell designs (Figs. 6a and 6c). Similarly, at the higher band, from 29 to 34 GHz, R_LL and R_RR are greater than −1 dB for most of the cell designs (Figs. 6f and 6h). At both bands, the cross-polarized CP reflection magnitudes, i.e., R_LR and R_RL, are below −10 dB (Figs. 6e and 6j). Regarding the co-polarized CP reflection phases, i.e., $\phi(r_\mathrm{LL})$ and $\phi(r_\mathrm{RR})$, the 16 cell designs can be divided

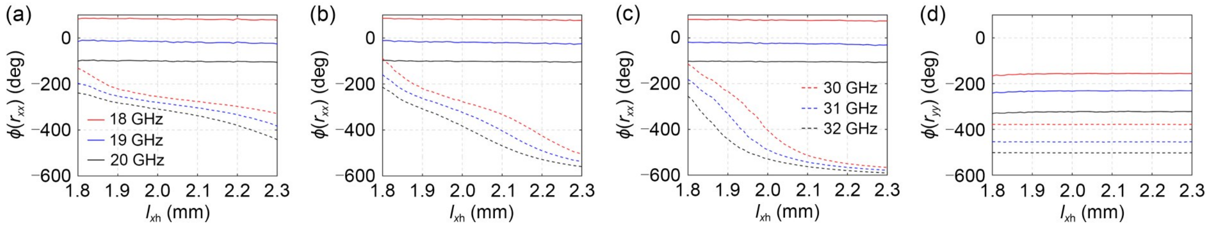

Fig. 5 Simulated $\phi(r_{xx})$ of RA cell B for r_h=0.7 (a), r_h=0.8 (b), and r_h=0.9 (c), as well as simulated $\phi(r_{yy})$ of RA cell B (d) at K-band (18, 19, and 20 GHz, as shown by solid lines) and Ka-band (30, 31, and 32 GHz, as shown by dashed lines) as a function of $l_{x\mathrm{h}}$. References to color refer to the online version of this figure

into four groups. At the lower band, each group contains curves that have the same line shape but different colors (Figs. 6b and 6d), whereas each group has curves with the same color but different line shapes at the higher band (Figs. 6g and 6i). At both bands, a phase difference of about 45° can be observed between the reflection phase curves belonging to different groups. Although the four groups can cover a phase range of 135°, a total phase range of 315° can be reached by simply introducing a 90° rotation to all the cells, thereby achieving a 3-bit phase resolution. It should be noted that, without element-rotation-induced phase delays, $\phi(r_{\mathrm{LL}})$ and $\phi(r_{\mathrm{RR}})$ are constrained to be the same.

In the third step, both the K- and Ka-band elements are rotated around their own geometrical centers by a certain angle of $\phi_{r\mathrm{l}}$ and $\phi_{r\mathrm{h}}$, respectively, to introduce the rotation phase that can distinguish between RCP- and LCP-reflected waves (Fig. 3c). The cell designs are denoted as RA cell C. Since the lower- and higher-band elements are aligned in an interleaved manner, the end-to-end distance between the dipoles is greater than 0.9 mm, with the smallest case happening when $l_{x\mathrm{l}}$=3.9 mm, $l_{x\mathrm{h}}$=2.27 mm, $\phi_{r\mathrm{l}}$=45°, and $\phi_{r\mathrm{h}}$=45°. This ensures that the capacitive coupling between the elements is weak enough, so that the response of the dipoles will not be affected when the elements are rotated. As shown in Figs. 7a and 7b, when the K- and Ka-band elements are rotated by an angle gradually increasing from −90.0° to 67.5° with a step of 22.5°, the co-polarized RCP and LCP reflection phases vary with opposite trends. At each band, and for each particular single value of the RCP/LCP reflection phase, four values of the reflection phase for the CP waves with the opposite handedness, i.e., the LCP/RCP waves, can be independently selected with a step of about 90°, meaning that a 2×2-bit dual-band dual-CP phase shift can be achieved.

2.4 Oblique incidence performance

To evaluate the angular stability of the phase shifting performance of the unit cells, the simulated reflection

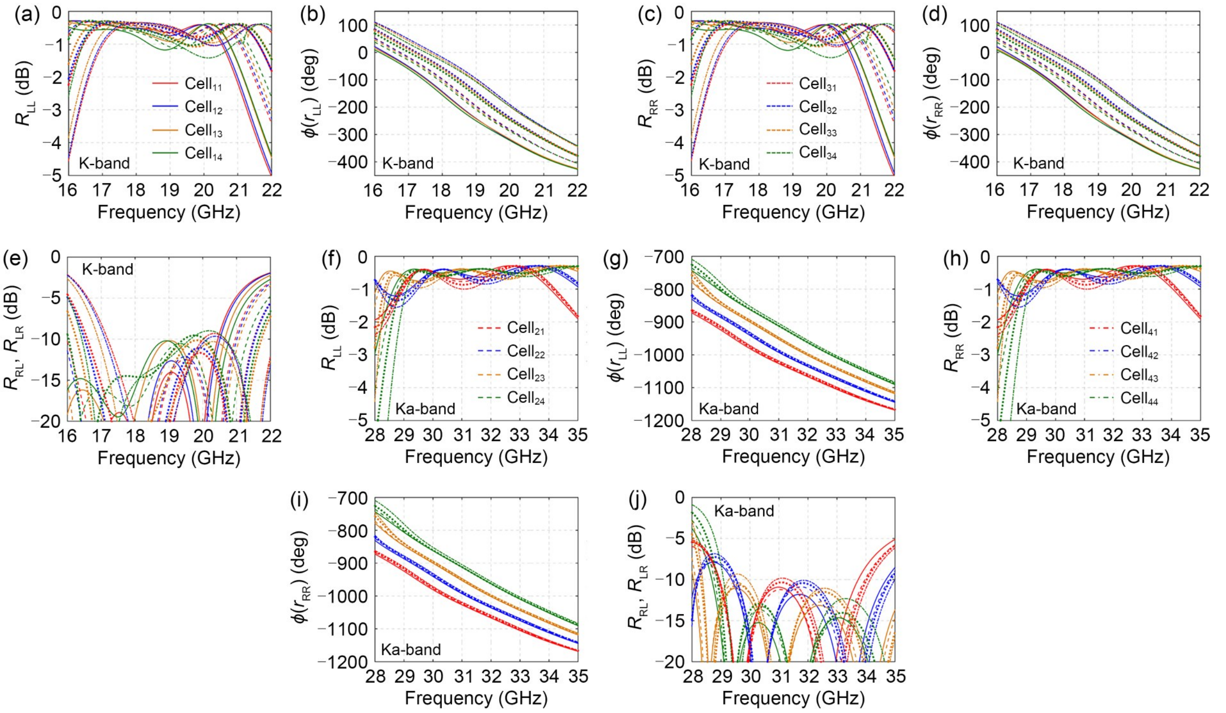

Fig. 6 Simulated co-polarized CP reflection magnitudes R_{LL} (a) and R_{RR} (c), simulated co-polarized CP reflection phases $\phi(r_{\mathrm{LL}})$ (b) and $\phi(r_{\mathrm{RR}})$ (d), and simulated cross-polarized CP reflection magnitudes R_{RL} and R_{LR} (e) of Cell$_{mn}$ with m=1, 2, 3, 4, i.e., $l_{x\mathrm{l}}$=3.9, 3.8, 3.7, 3.6 mm, and n=1, 2, 3, 4, i.e., $l_{x\mathrm{h}}$=2.27, 2.21, 2.15, 2.09 mm at K-band; simulated co-polarized CP reflection magnitudes R_{LL} (f) and R_{RR} (h), simulated co-polarized CP reflection phases $\phi(r_{\mathrm{LL}})$ (g) and $\phi(r_{\mathrm{RR}})$ (i), and simulated cross-polarized CP reflection magnitudes R_{RL} and R_{LR} (j) of Cell$_{mn}$ with m=1, 2, 3, 4, i.e., $l_{x\mathrm{l}}$=3.9, 3.8, 3.7, 3.6 mm, and n=1, 2, 3, 4, i.e., $l_{x\mathrm{h}}$=2.27, 2.21, 2.15, 2.09 mm at Ka-band. References to color refer to the online version of this figure

properties of the dual-band dual-CP RA cells as a function of the incident angle are investigated. For simplicity, the results of two out of the 16 cell designs are illustrated, which are Cell$_{42}$ (formed by Ele$_{\mathrm{L4}}$ and Ele$_{\mathrm{H2}}$) with $l_{x\mathrm{l}}$=3.6 mm, $l_{x\mathrm{h}}$=2.21 mm, $\phi_{r\mathrm{l}}$=45.0°, $\phi_{r\mathrm{h}}$=−22.5°, and Cell$_{34}$ (formed by Ele$_{\mathrm{L3}}$ and Ele$_{\mathrm{H4}}$) with $l_{x\mathrm{l}}$=3.7 mm, $l_{x\mathrm{h}}$=1.69 mm, $\phi_{r\mathrm{l}}$=67.5°, $\phi_{r\mathrm{h}}$=22.5°. As can be seen from Figs. 8a and 8b, with the plane of incidence defined to be the x−z plane, at both 19 and 31 GHz, the co-polarized CP reflection magnitudes are around −0.5 dB in the range of incident angles from 0° to 30° for both cells. The undesirable cross-polarized CP reflection magnitudes are below −14 dB for most of the incident angles. The co-polarized CP transmission phases for both the LCP and RCP incident waves remain almost constant as the angle of incidence changes, with a variation of less than 10°, indicating a stable phase shift within the field-of-view.

Importantly, due to the weak coupling between the K- and Ka-band elements, the CP reflection magnitudes and phases are well maintained for different angles of incidence. At larger incident angles beyond 30°, Cell$_{42}$ exhibits slightly degraded performance at the higher band, when compared to Cell$_{34}$. Nevertheless, the variations of its co-polarized CP reflection magnitude and phase are still maintained within an

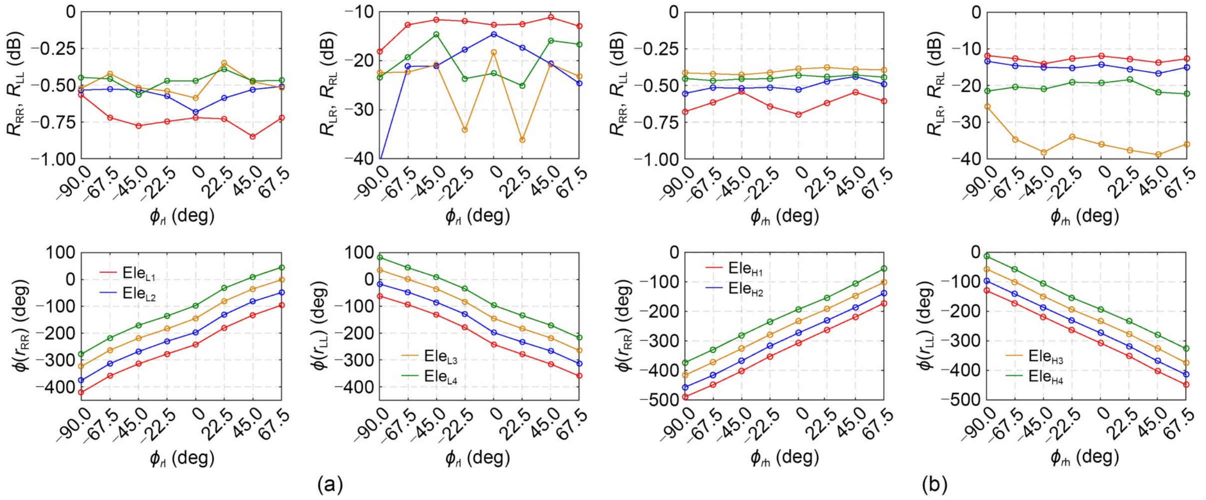

Fig. 7 Simulated co-polarized CP reflection magnitudes (R_{LL} and R_{RR}), cross-polarized CP reflection magnitudes (R_{LR} and R_{RL}), and co-polarized CP reflection phases ($\phi(r_{\mathrm{LL}})$ and $\phi(r_{\mathrm{RR}})$) at 19 GHz as a function of $\phi_{r\mathrm{l}}$ (a) and 31 GHz as a function of $\phi_{r\mathrm{h}}$ (b). References to color refer to the online version of this figure

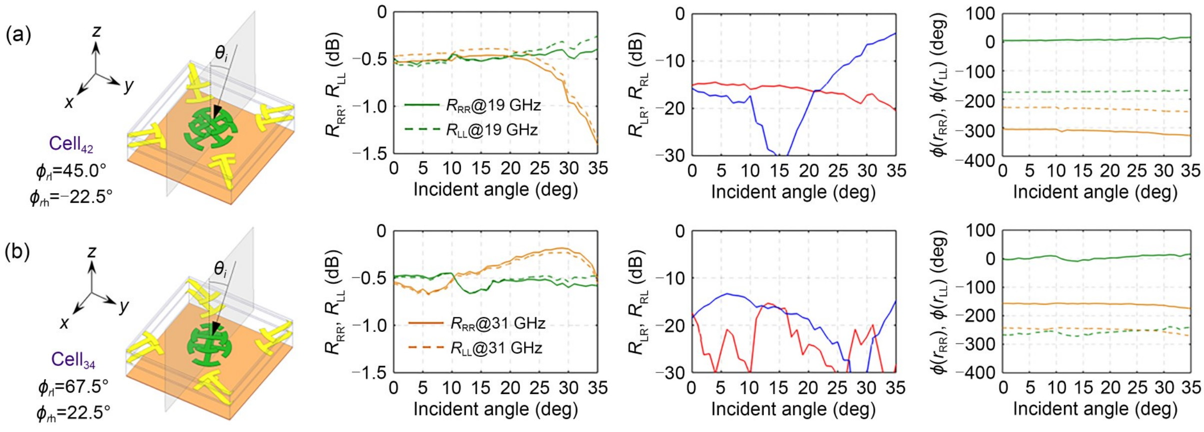

Fig. 8 Three-dimensional (3D) view of the dual-band dual-CP RA cells illuminated by an obliquely incident plane wave and simulated co-polarized CP reflection magnitudes (R_{LL} and R_{RR}), cross-polarized CP reflection magnitudes (R_{LR} and R_{RL}), and co-polarized CP reflection phases ($\phi(r_{\mathrm{LL}})$ and $\phi(r_{\mathrm{RR}})$) for Cell$_{42}$ with $\phi_{r\mathrm{l}}$=45.0°, $\phi_{r\mathrm{h}}$=−22.5° (a) and Cell$_{34}$ with $\phi_{r\mathrm{l}}$=67.5°, $\phi_{r\mathrm{h}}$=22.5° (b)

acceptable range. Such properties confirm that the designed dual-band dual-CP RA cells have a robust performance within an angular cone of 35°. This is almost equal to the incident angle for the edge elements in the RA designed later and, hence, is critical for the realization of the final dual-band dual-CP RAs with a relatively small F/D ratio.

3 Broadband K- and Ka-band dual-CP planar feeds

For most previously reported RAs and TAs, horn antennas have been used as the feed sources, which greatly increases the overall profile of the final device, especially for CP horns due to the use of long waveguide circular polarizers (Luo et al., 2019; Jiang et al., 2020a; Naseri et al., 2020). Here, as alternatives, two planar dual-CP feeds, one operating at the K-band and the other at the Ka-band, are employed, both having two input ports for exciting LCP- and RCP-radiated waves over a wide band. This scheme is also amenable for system applications in the sense that they are lightweight and more straightforward for connection with other planar front-end circuits. In this section, the design and validation of broadband dual-port dual-CP planar feeds that operate at K- and Ka-band will be presented.

The configuration of the K- and Ka-band planar feeds (Fig. 9a), placed side by side, contains four dielectric and four metallic layers. The top three substrate layers consist of Taconic TLY-5. Each feed consists of a dual-polarized magneto-electric dipole fed by two orthogonal L-shaped probes connected to two microstrip lines beneath the ground plane (Li YJ et al., 2017). The feeding microstrip lines, printed on a Rogers RO4003 substrate with a thickness of $t_{\mathrm{K1}}=t_{\mathrm{Ka1}}=0.203$ mm, have a characteristic impedance of 50 Ω (Fig. 9b). To achieve broadband dual-CP radiation, two second-order hybrid couplers are implemented using microstrip lines, one operating at the K-band and the other at the Ka-band (Muraguchi et al., 1983). The detailed geometrical dimensions of the radiators and couplers are provided in Figs. 9c and 9d. By exciting the two input ports of the coupler, the phase difference between the two output ports is 90° or −90°, resulting in RCP or LCP radiation, respectively.

The two feeds are fabricated and characterized, and Southwest end launch connectors are used to connect the prototypes to the network analyzer. When the two feeds are placed side by side, the center-to-center distance is about 24 mm. The simulated and measured S-parameters as a function of frequency are displayed in Figs. 10a and 10b, where a good agreement between them can be observed. The measured reflection magnitudes of all four input ports, i.e., S_{nn} with n=1, 2, 3, 4, are below −13 dB over a broad band from 16 to 22 GHz at the K-band and from 28 to 35 GHz at the Ka-band. The mutual coupling between co-band cross-polarized ports, i.e., S_{21} and S_{43}, have measured values below −13 and −17 dB, respectively, at the lower and higher bands. For cross-band coupling, i.e., S_{31}, S_{32}, S_{41}, and S_{42}, the measured maximum values are all smaller than −30 dB, thus almost negligible. The radiation properties of the feeds are measured in a far-field anechoic chamber. The simulated and measured

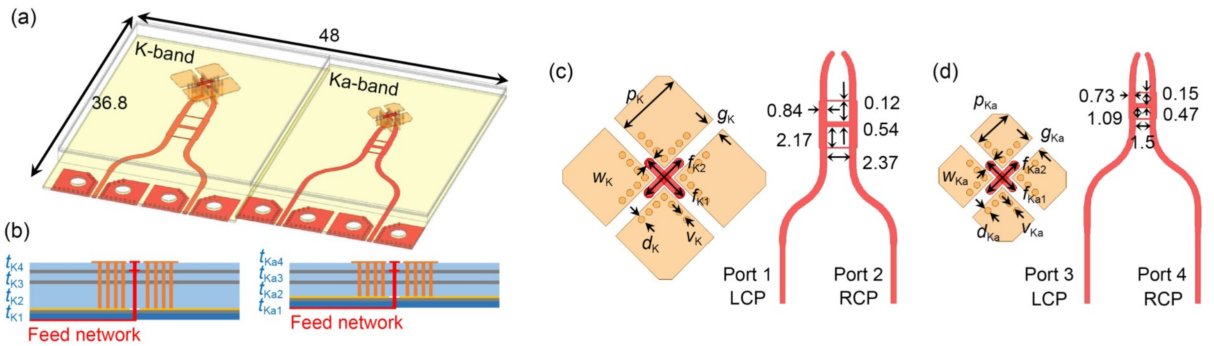

Fig. 9 Configuration (a) and side views (b) of the broadband dual-CP planar feeds operating at K- and Ka-band; planar views of the K-band (c) and Ka-band (d) magnetoelectric dipoles and broadband microstrip hybrid couplers. The geometrical dimensions are t_{K1}=0.203, t_{K2}=1.52, t_{K3}=0.13, t_{K4}=0.25, p_{K}=3.04, g_{K}=0.6, v_{K}=0.17, d_{K}=0.3, f_{K1}=2.34, f_{K2}=2.31, w_{K}=0.4, t_{Ka1}=0.203, t_{Ka2}=0.76, t_{Ka3}=0.13, t_{Ka4}=0.25, p_{Ka}=1.87, g_{Ka}=0.60, v_{Ka}=0.17, d_{Ka}=0.28, f_{Ka1}=1.79, f_{Ka2}=1.94, and w_{Ka}=0.38, all in millimeters

peak CP gain and AR values as a function of frequency are shown in Figs. 10c and 10d when only a single port is excited with the others terminated by matched loads of 50 Ω. For the two K-band ports, it can be seen that the RCP- and LCP-radiated beams have a measured AR of smaller than 2 dB in the majority of the band from 16 to 22 GHz, i.e., a bandwidth of 31.6%, with a maximum AR of about 2.3 dB (Fig. 10c). Correspondingly, the measured peak RCP and LCP gain values vary between 7.0 and 7.6 dBic, while the radiated beams possess a half-power beamwidth (HPBW) of about 75° in different φ planes by virtue of the good beam shape symmetry of the employed magneto-electric dipole (Li YJ et al., 2017). For the two ports at the Ka-band, in the frequency range from 27 to 35 GHz, i.e., a bandwidth of 25.9%, the measured AR values of the RCP and LCP beams are below 2.1 dB, while the peak CP gain fluctuates from about 8.0 to 7.2 dBic (Fig. 10d). The HPBW of the CP beams emitted from the Ka-band feed is about 73°. Overall, the measurement results of the dual-CP planar feeds agree well with the simulation predictions, exhibiting a stable gain and high polarization purity over a broad band that can cover the operational bands of the RA cells. Their moderate gain implies that they can facilitate the design of integrated RAs with smaller *F*/*D* ratios.

4 Design and experimental validation of the dual-band dual-CP RA integrated with dual-CP planar feeds

In this section, an integrated dual-band dual-CP RA antenna operating at the K- and Ka-band is synthesized, based on the designed dual-band dual-CP RA cells and the broadband dual-CP planar feeds. Different from the previously reported single- and dual-band dual-CP RA/TA systems, where CP feeds with different handedness are required for generating RCP and LCP beams (Jiang et al., 2021; Tong et al., 2022), the designed and demonstrated RA can provide four CP beams simultaneously by exciting different input ports, thereby offering true dual-band dual-CP operation with four degrees of freedom. By employing the planar dual-band dual-CP radiator as the feed source, the RA antenna has the following advantages: (1) the planar radiator can be readily connected to other planar front-end circuits; (2) the total profile of the RA can be significantly reduced; (3) the aperture size of the planar feeds is smaller than that of the horn antennas, and thereby the feed blockage can be reduced. To achieve a gain of higher than 24 dBic, the diameter of the quasi-circular RA is set to be 160 mm, i.e., about 10.1λ_0 at 19 GHz and 16.5λ_0 at 31 GHz, containing a total of 796 K-band elements and 749 Ka-band

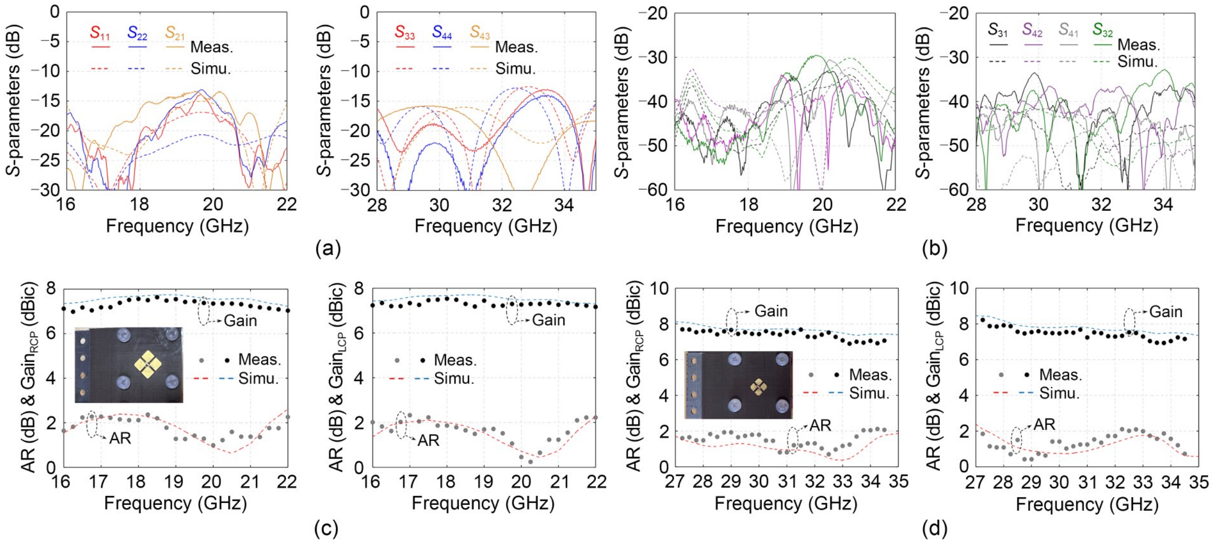

Fig. 10 (a) Simulated and measured port reflection magnitudes and mutual coupling between co-band cross-polarized ports of the dual-CP feeds at K- and Ka-band; (b) simulated and measured mutual coupling between cross-band ports of the dual-CP feeds at K- and Ka-band; simulated and measured AR and gain of the radiated CP wave achieved by exciting the RCP and LCP ports of the K-band feed (c) and the RCP and LCP ports of the Ka-band feed (d). References to color refer to the online version of this figure

elements. An F/D ratio of 0.65, i.e., F=104 mm, is chosen to ensure a relatively small overall profile such that the cells on the edge of the RA elements are illuminated by waves with an angle of incidence of about 37° (Fig. 1).

4.1 Dual-band dual-CP RA design

As a proof-of-concept demonstration, an exemplary design providing four directive beams asymmetrically distributed in the two orthogonal planes, i.e., x–z and y–z planes, is considered here. At 19 and 31 GHz, the targeted beam directions for the LCP and RCP beams in the lower and higher bands are $(\theta_\mathrm{L}, \varphi_\mathrm{L})_\mathrm{K}$=(−30°, 0°), $(\theta_\mathrm{R}, \varphi_\mathrm{R})_\mathrm{K}$=(30°, 90°), $(\theta_\mathrm{L}, \varphi_\mathrm{L})_\mathrm{Ka}$=(−20°, 90°), and $(\theta_\mathrm{R}, \varphi_\mathrm{R})_\mathrm{Ka}$=(20°, 0°). To achieve such a dual-band dual-CP functionality generating four independent beams, the dual-band dual-CP RA cells are used to compensate for the inhomogeneous phases of the incident waves across the RA aperture and impose additional phase gradients for beam steering. The resulting distributions of the element number and in-plane rotation angle (ϕ_{rl} and ϕ_{rh}) of the K- and Ka-band elements of the RA cells are shown in Fig. 11a. In the full-wave simulation setup of the integrated RA antenna using HFSS, a hybrid finite element–boundary integral (FE–BI) method is employed, which greatly reduces the consumed computational resources (Jin and Volakis, 1991).

The normalized simulated CP patterns in the two orthogonal planes containing the main beams at 19 and 31 GHz are displayed in Figs. 12a and 12b, respectively. It can be seen that LCP pencil beams are produced at −30° in the x–z plane for the K-band and −20° in the y–z plane for the Ka-band. When the RCP ports of the feeds are excited, directive RCP beams can be observed pointing at 30° in the y–z plane and 20° in the x–z plane at 19 and 31 GHz, respectively. For all four beams, the strength of the orthogonally-polarized wave is below −22 dB. The beam gain and AR as a function of frequency are shown in Figs. 13a and 13b. The simulated AR is smaller than 2 dB for both RCP and LCP beams in the frequency bands spanning from 16.3 to 21.1 GHz and from 28.1 to 35.0 GHz. The simulated joint 1-dB gain and AR<2 dB bandwidths of the RA are about 21% and 15% for the CP beams for the K- and Ka-band, respectively. The simulated gain curves exhibit quite flattened line-shapes for both the RCP/LCP beams, which have peak values of around 24.6/24.4 dBic and 27.5/27.4 dBic in the K- and Ka-band, respectively. The corresponding simulated aperture

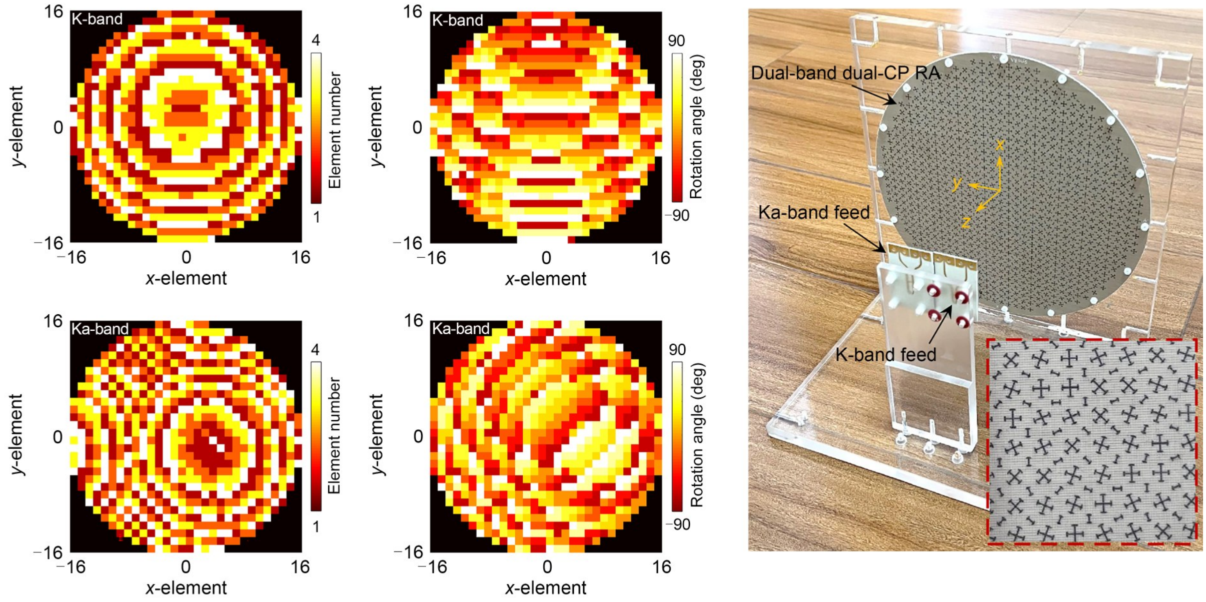

(a) (b)

Fig. 11 (a) Element number and rotation angle distributions of the K- and Ka-band elements of the dual-band dual-CP RA design; (b) photograph of the dual-band dual-CP RA prototype integrated with the broadband dual-CP planar feeds. The inset shows an enlarged view of a portion of the top metallic layer of the RA

efficiencies are around 27.93% and 20.70% at the lower and higher frequency bands. To estimate the aperture efficiency of the finite-sized RA, the detailed loss budgets at the lower and higher bands are listed in Table 1. As can be seen, the sum of the loss is about 5.54 dB (6.84 dB), indicating an aperture efficiency of 27.9% (20.7%) at the K-band (Ka-band). The main loss of the designed RA is the spillover loss caused by the large HPBW of the feed source, which can be reduced by using an antenna array or a small horn as the feed of the RA.

It can be seen that the dual-band dual-CP RA design, although with different beam pointing directions, possesses beam squinting for the LCP and RCP beams of less than 4° within the joint 1-dB gain and AR<2 dB bandwidths (Fig. 13c). The amount of squinting for beams pointing at smaller angles of ±20° is less than 3°. In addition, the simulated reflection coefficients for the

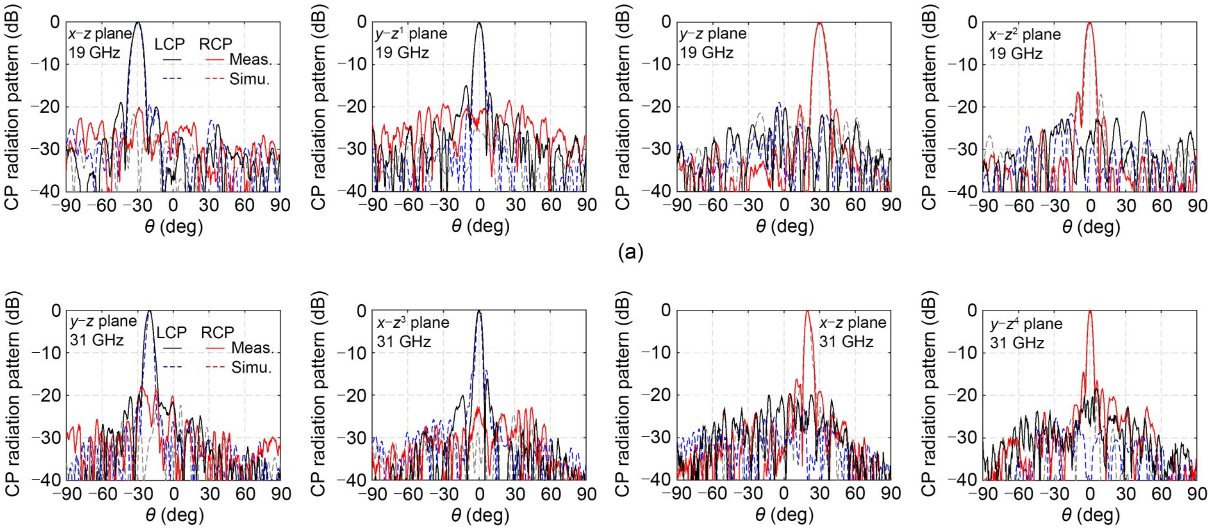

(a)

(b)

Fig. 12 Simulated and measured normalized CP radiation patterns in the two orthogonal planes cutting through the main beam of the dual-band dual-CP RA at 19 GHz (a) and 31 GHz (b), where z^1=$z$cos 30°–$x$sin 30°, z^2=$z$cos 30°+$y$sin 30°, z^3=$z$cos 20°–$y$sin 20°, and z^4=$z$cos 20°+$x$sin 20°

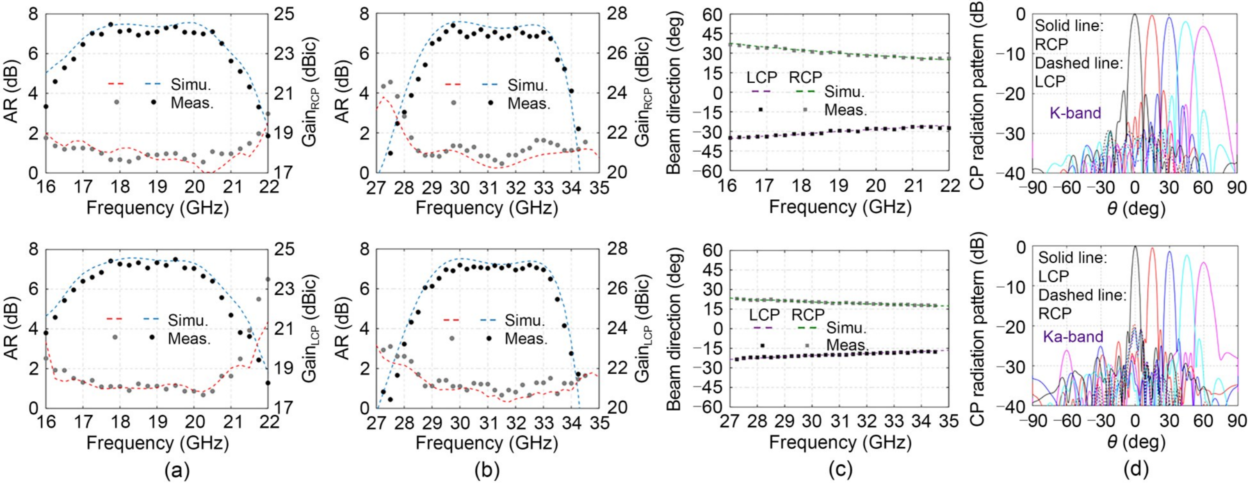

Fig. 13 Simulated and measured peak gain and AR as a function of frequency for the dual-band dual-CP RA for the K-band (a) and Ka-band (b); (c) simulated and measured beam directions for the dual-band dual-CP RA antenna as a function of frequency; (d) performance of the K-band RCP beam (top) and Ka-band LCP beam (bottom) with different pointing angles of the RA antenna

Table 1 Simulated constituents of aperture efficiency

Efficiency type	Value (%)		Loss (dB)	
	K-band	Ka-band	K-band	Ka-band
Radiation efficiency	93.11	91.62	0.31	0.38
Spillover efficiency	47.75	44.26	3.21	3.54
Illumination efficiency	75.34	72.11	1.23	1.42
Phase quantization efficiency	95.94	95.94	0.18	0.18
Cell reflection efficiency	89.13	85.11	0.50	0.70
Oblique incidence efficiency	97.50	86.70	0.11	0.62
Total aperture efficiency	27.93	20.70	5.54	6.84

RA design are below −13 dB within the bands of interest (not shown here for brevity), which are almost the same as those of the feeds alone.

To evaluate the performance of the generated beam when it is pointed to large angles, the K-band RCP (Ka-band LCP) beams with different directions in the y–z (x–z) plane from 0° to 60° at an interval of 15° are presented in Fig. 13d, while keeping the K-band LCP (Ka-band RCP) beam directed to $(\theta_L, \varphi_L)_K$=(−30°, 0°) ($(\theta_R, \varphi_R)_{Ka}$=(0°, 0°)). As can be seen from Fig. 13d, the gain drops by only about 3.2 dB for the K-band RCP beam pointing at 60° compared with the beam directed at 0°. In addition, the cross-polarization levels are lower than −30 dB for all the beams with different pointing angles, which indicates that the AR performance is satisfying. For the Ka-band LCP beams, the gain decreases by about 4.1 dB for the beam pointing at 60° compared with the beam directed at 0°, which is a bit more than that of the K-band beam. This is caused mainly by the larger element spacing at the Ka-band. Moreover, the cross-polarization levels are lower than −20 dB, which means that the AR values are all lower than 3 dB for all the beams. As a conclusion, benefiting from the small element spacing, the K- and Ka-band beams can even deflect to angles as large as 60° with a stable performance.

4.2 Experimental results and discussions

The designed dual-band dual-CP RA is fabricated and assembled with the two corresponding dual-CP planar feeds. A frame made of glass is built to precisely control the relative positions of the feeds and the RA panel (Fig. 11b). The inset shows an enlarged view of the top metallic layer of the RA. During the measurements, when one port of the feeds is excited, the others are terminated by matched loads of 50 Ω.

For the dual-band dual-CP RA that generates two RCP and two LCP beams distributed asymmetrically in the x–z and y–z planes, the measured normalized patterns are displayed in Fig. 12. At 19 GHz, the RA experimentally produces an RCP beam pointing at 30.0° in the y–z plane and an LCP beam directed at −30.1° in the x–z plane. At 31 GHz, the generated RCP beam radiates towards 20.0° in the x–z plane, while a directive LCP beam points at −20.1° in the y–z plane. The measured peak gain values for the RCP/LCP beams are 24.5/24.3 dBic and 27.3/27.1 dBic, respectively, corresponding to measured aperture efficiencies of about 26.9% and 19.8%. As reported in Figs. 13a and 13b, the measured joint 1-dB gain and AR<2 dB bandwidth is, on average, about 20.6% and 14.6% for the CP beams in the K- and Ka-band, respectively. Within these bands, the measured beam direction has a variation of less than 3.8° and 3.2° for the CP beams pointing at 30° and 20° from the normal direction, respectively (Fig. 13c).

In all, the measurement results confirm the dual broadband properties of the proposed dual-band dual-CP RA integrated with planar dual-CP feeds. The demonstrated RA can achieve desirable beamforming with independent control of waves of opposite circular-polarizations or at different frequencies, using only a single functional layer. As illustrated in Table 2, compared to previously reported dual-band dual-CP RAs (Luo et al., 2019; Naseri et al., 2020; Xu et al., 2021; Tong et al., 2022), the proposed and validated RA enabled by multi-layered phase shifting surfaces possesses a greatly extended bandwidth, higher aperture efficiency, and smaller panel thickness. Their

Table 2 Comparisons with previously reported dual-band dual-CP RAs

Reference	Phase shifting technique	Operating frequency	RA panel thickness*	F/D ratio	Feed	Element spacing	Peak gain (dBic)**	Aperture efficiency**	1-dB gain & AR<2 dB BW**
Luo et al., 2019	Dynamic phase	8.6 & 10.1 GHz	$0.024\lambda_L$	0.58	Horn antenna	22.5 mm ($0.64\lambda_L/0.75\lambda_H$)	16.9/19.0	10.6%/17.9%	<3%/<3%***
							18.3/17.7	11.6%/10.3%	<2%/<2%
Naseri et al., 2020	Dynamic phase	18.2 & 27.3 GHz	$1.23\lambda_L$	0.94	Horn antenna	5.3 mm ($0.32\lambda_L/0.48\lambda_H$)	29.2/29.1	22.8%/22.3%	2.2%/2.2%***
							30.1/30.5	12.5%/13.7%	2.6%/2.9%
Xu et al., 2021	Dynamic+rotation phases	12.5 & 30 GHz	$0.52\lambda_L$	0.90	Horn antenna	10 mm/5 mm ($0.42\lambda_L/0.5\lambda_H$)	25.6/25.3	14.5%/13.8%	2.7%/5.8%
							31.0/32.1	13.8%/15.6%	<4%/<3%
Tong et al., 2022	Dynamic+rotation phases	20 & 30 GHz	$0.27\lambda_L$	1.25	Horn antenna	6 mm ($0.4\lambda_L/0.6\lambda_H$)	27.0/27.0	35.0%/35.0%	7.3%/7.2%
							28.0/28.5	20.9%/23.9%	6.7%/6.6%
This work	Dynamic+rotation phases	19 & 31 GHz	$0.1\lambda_L$	0.65	Planar radiators	5 mm ($0.31\lambda_L/0.51\lambda_H$)	24.3/24.4	26.6%/27.2%	20.6%/21.0%
							27.2/27.3	19.5%/20.0%	14.6%/14.7%

* λ_L is the free-space wavelength at the lower band; ** The data before and after "/" represent the RCP and LCP beam performance respectively, and the first and second rows for each work represent the lower- and higher-band performance respectively; *** The results reported for these two works represent their 1-dB gain and AR<3.5 dB bandwidth

small F/D ratio, along with the use of planar feeds, also makes the overall profile of the RA antenna more compact.

5 Conclusions

This paper reported the design and demonstration of the dual-broadband dual-CP RA integrated with dual-CP planar feeds. By jointly exploiting the dynamic and rotation phase compensation and interleaving K-/Ka-band multi-layered phase shifting elements in a shared aperture, independent phase shifts for RCP and LCP waves at both bands can be accomplished with a profile of only about $0.1\lambda_L$. A proof-of-concept dual-band dual-CP RA integrated with dual-CP planar feeds was synthesized, fabricated, and characterized. The measured peak gains were greater than 24 and 27 dBic at the K- and Ka-band, respectively. The experimentally achieved joint 1-dB gain and AR<2 dB bandwidths were close to 21% and 15% at the two operational bands, respectively. The demonstrated low-profile dual-broadband dual-CP RA is a promising candidate for satellite and space communication systems.

Contributors

Zhi Hao JIANG and Wei HONG supervised the project. Xuanfeng TONG performed numerical simulations and experiments. Xuanfeng TONG and Zhi Hao JIANG drafted the paper. Yuan LI, Fan WU, Lin PENG, and Taiwei YUE contributed to data interpretation and manuscript revision.

Conflict of interest

The authors declare that they have no conflict of interest.

Data availability

The data that support the findings of this study are available from the corresponding author upon reasonable request.

References

Abdelrahman AH, Yang F, Elsherbeni AZ, et al., 2017. Analysis and Design of Transmitarray Antennas. Springer, Cham, Germany. https://doi.org/10.1007/978-3-031-01541-0

Amendola G, Cavallo D, Chaloun T, et al., 2023. Low-Earth orbit user segment in the Ku and Ka-band: an overview of antennas and RF front-end technologies. *IEEE Microw Mag*, 24(2):32-48. https://doi.org/10.1109/MMM.2022.3217961

Chaharmir MR, Shaker J, 2015. Design of a multilayer X-/Ka-band frequency-selective surface-backed reflectarray for satellite applications. *IEEE Trans Antenn Propag*, 63(4):1255-1262. https://doi.org/10.1109/TAP.2015.2389838

Cheng CC, Abbaspour-Tamijani A, 2009. Evaluation of a novel topology for MEMS programmable reflectarray antennas. *IEEE Trans Microw Theory Tech*, 57(12):3333-3344. https://doi.org/10.1109/TMTT.2009.2034420

Deng RY, Xu SH, Yang F, et al., 2017a. Design of a low-cost single-layer X/Ku dual-band metal-only reflectarray antenna. *IEEE Antenn Wirel Propag Lett*, 16:2106-2109. https://doi.org/10.1109/LAWP.2017.2698099

Deng RY, Xu SS, Yang F, et al., 2017b. Single-layer dual-band reflectarray antennas with wide frequency ratios and high aperture efficiencies using phoenix elements. *IEEE Trans Antenn Propag*, 65(2):612-622. https://doi.org/10.1109/TAP.2016.2639023

Deng RY, Yang F, Xu SH, et al., 2017c. An FSS-backed 20/30-GHz dual-band circularly polarized reflectarray with suppressed mutual coupling and enhanced performance. *IEEE Trans Antenn Propag*, 65(2):926-931. https://doi.org/10.1109/TAP.2016.2633159

Deng RY, Xu SH, Yang F, et al., 2018. An FSS-backed Ku/Ka quad-band reflectarray antenna for satellite communications. *IEEE Trans Antenn Propag*, 66(8):4353-4358. https://doi.org/10.1109/TAP.2018.2835725

Encinar JA, Zornoza JA, 2003. Broadband design of three-layer printed reflectarrays. *IEEE Trans Antenn Propag*, 51(7): 1662-1664. https://doi.org/10.1109/TAP.2003.813611

Fenech H, 2021. High-Throughput Satellites. Artech, Norwood, USA.

Fenech H, Amos S, Tomatis A, et al., 2015. High throughput satellite systems: an analytical approach. *IEEE Trans Aerosp Electron Syst*, 51(1):192-202. https://doi.org/10.1109/TAES.2014.130450

Florencio R, Encinar JA, Boix RR, et al., 2019. Flat reflectarray that generates adjacent beams by discriminating in dual circular polarization. *IEEE Trans Antenn Propag*, 67(6): 3733-3742. https://doi.org/10.1109/TAP.2019.2905676

Gagnon N, Petosa A, McNamara DA, 2013. Research and development on phase-shifting surfaces (PSSs). *IEEE Antenn Propag Mag*, 55(2):29-48. https://doi.org/10.1109/MAP.2013.6529314

Garcia-Aguilar A, Inclan-Alonso JM, Vigil-Herrero L, et al., 2012. Low-profile dual circularly polarized antenna array for satellite communications in the X band. *IEEE Trans Antenn Propag*, 60(5):2276-2284. https://doi.org/10.1109/TAP.2012.2189729

Geaney CS, Hosseini M, Hum SV, 2019. Reflectarray antennas for independent dual linear and circular polarization control. *IEEE Trans Antenn Propag*, 67(9):5908-5918. https://doi.org/10.1109/TAP.2019.2916596

Guo WL, Wang GM, Ji WY, et al., 2020. Broadband spin-decoupled metasurface for dual-circularly polarized reflector antenna design. *IEEE Trans Antenn Propag*, 68(5): 3534-3543. https://doi.org/10.1109/TAP.2020.2963945

Hong W, Jiang ZH, Yu C, et al., 2021. The role of millimeter-wave technologies in 5G/6G wireless communications. *IEEE J Microw*, 1(1):101-122. https://doi.org/10.1109/JMW.2020.3035541

Huang J, Encinar JA, 2008. Reflectarray Antennas. Wiley, Hoboken, USA.

Jiang ZH, Yue TW, Hong W, 2020a. Low-profile and wide-band dual-circularly polarized reflect-arrays based on rotated metal-backed dual-polarized aperture-coupled patch elements. *IEEE Trans Antenn Propag*, 68(3):2108-2117. https://doi.org/10.1109/TAP.2019.2948564

Jiang ZH, Zhang Y, Hong W, 2020b. Anisotropic impedance surface-enabled low-profile broadband dual-circularly polarized multibeam reflectarrays for Ka-band applications. *IEEE Trans Antenn Propag*, 68(8):6441-6446. https://doi.org/10.1109/TAP.2020.2975263

Jiang ZH, Wu F, Yue TW, et al., 2021. Wideband and low-profile integrated dual-circularly-polarized transmit-arrays enabled by antenna-filter-antenna phase shifting cells. *IEEE Trans Antenn Propag*, 69(11):7462-7475. https://doi.org/10.1109/TAP.2021.3076586

Jin JM, Volakis JL, 1991. A finite-element-boundary integral formulation for scattering by three-dimensional cavity-backed apertures. *IEEE Trans Antenn Propag*, 39(1): 97-104. https://doi.org/10.1109/8.64442

Joyal MA, El Hani R, Riel M, et al., 2015. A reflectarray-based dual-surface reflector working in circular polarization. *IEEE Trans Antenn Propag*, 63(4):1306-1313. https://doi.org/10.1109/TAP.2014.2388204

Li Y, Jiang ZH, Tong XF, et al., 2022. Wideband dual-circularly-polarized reflect-arrays based on dual-functional-layer cells with Berry-phase compensation at X-band. *IEEE Trans Antenn Propag*, 70(10):9924-9929. https://doi.org/10.1109/TAP.2022.3184536

Li YJ, Wang JH, Luk KM, 2017. Millimeter-wave multibeam aperture-coupled magnetoelectric dipole array with planar substrate integrated beamforming network for 5G applications. *IEEE Trans Antenn Propag*, 65(12):6422-6431. https://doi.org/10.1109/TAP.2017.2681429

Liu N, Sheng XJ, Zhang CB, et al., 2017. A miniaturized tri-band frequency selective surface based on convoluted design. *IEEE Antenn Propag Lett*, 16:2384-2387. https://doi.org/10.1109/LAWP.2017.2719859

Luo Q, Gao S, Sobhy M, et al., 2016. Dual circularly polarized equilateral triangular patch array. *IEEE Trans Antenn Propag*, 64(6):2255-2262. https://doi.org/10.1109/TAP.2016.2551260

Luo Q, Gao S, Li WT, et al., 2019. Multibeam dual-circularly polarized reflectarray for connected and autonomous vehicles. *IEEE Trans Veh Technol*, 68(4):3574-3585. https://doi.org/10.1109/TVT.2019.2897218

Malfajani RS, Atlasbaf Z, 2014. Design and implementation of a dual-band single layer reflectarray in X and K bands. *IEEE Trans Antenn Propag*, 62(8):4425-4431. https://doi.org/10.1109/TAP.2014.2327137

Mao CX, Jiang ZH, Werner DH, et al., 2019. Compact self-diplexing dual-band dual-sense circularly polarized array antenna with closely spaced operating frequencies. *IEEE Trans Antenn Propag*, 67(7):4617-4625. https://doi.org/10.1109/TAP.2019.2911274

Martinez-de-Rioja D, Martinez-de-Rioja E, Rodriguez-Vaqueiro Y, et al., 2021. Transmit-receive parabolic reflectarray to generate two beams per feed for multispot satellite antennas in Ka-band. *IEEE Trans Antenn Propag*, 69(5):2673-2685. https://doi.org/10.1109/TAP.2020.3030942

Martinez-de-Rioja E, Martinez-de-Rioja D, Encinar JA, et al., 2019. Advanced multibeam antenna configurations based on reflectarrays: providing multispot coverage with a smaller number of apertures for satellite communications in the K and Ka bands. *IEEE Antenn Propag Mag*, 61(5):77-86. https://doi.org/10.1109/MAP.2019.2932311

Mener S, Gillard R, Sauleau R, et al., 2014. Unit cell for reflectarrays operating with independent dual circular polarizations. *IEEE Antenn Wirel Propag Lett*, 13:1176-1179. https://doi.org/10.1109/LAWP.2014.2330623

Mener S, Gillard R, Sauleau R, et al., 2015. Dual circularly polarized reflectarray with independent control of polarizations. *IEEE Trans Antenn Propag*, 63(4):1877-1881. https://doi.org/10.1109/TAP.2015.2398458

Muraguchi M, Yukitake T, Naito Y, 1983. Optimum design of 3-dB branch-line couplers using microstrip lines. *IEEE Trans Microw Theory Tech*, 31(8):674-678. https://doi.org/10.1109/TMTT.1983.1131568

Naseri P, Riel M, Demers Y, et al., 2020. A dual-band dual-circularly polarized reflectarray for K/Ka-band space applications. *IEEE Trans Antenn Propag*, 68(6):4627-4637. https://doi.org/10.1109/TAP.2020.2972650

Nayeri P, Yang F, Elsherbeni AZ, 2015. Beam-scanning reflectarray antennas: a technical overview and state of the art. *IEEE Antenn Propag Mag*, 57(4):32-47. https://doi.org/10.1109/MAP.2015.2453883

Sanz-Fernández J, Saenz E, de Maagt P, 2015. A circular polarization selective surface for space applications. *IEEE Trans Antenn Propag*, 63(6):2460-2470. https://doi.org/10.1109/TAP.2015.2414450

Selvanayagam M, Eleftheriades GV, 2016. Design and measurement of tensor impedance transmitarrays for chiral polarization control. *IEEE Trans Microw Theory Tech*, 64(2):414-428. https://doi.org/10.1109/TMTT.2015.2505718

Shamsaee Malfajani R, Abbasi Arand B, 2017. Dual-band orthogonally polarized single-layer reflectarray antenna. *IEEE Trans Antenn Propag*, 65(11):6145-6150. https://doi.org/10.1109/TAP.2017.2754459

Sheng M, Zhou D, Bai WG, et al., 2023. Coverage enhancement for 6G satellite-terrestrial integrated networks: performance metrics, constellation configuration and resource allocation. *Sci China Inform Sci*, 66(3):130303. https://doi.org/10.1007/s11432-022-3636-1

Smith T, Gothelf U, Kim OS, et al., 2013. Design, manufacturing, and testing of a 20/30-GHz dual-band circularly polarized reflectarray antenna. *IEEE Antenn Wirel Propag Lett*, 12: 1480-1483. https://doi.org/10.1109/LAWP.2013.2288995

Sofi MA, Saurav K, Koul SK, 2020. Frequency-selective surface-based compact single substrate layer dual-band transmission-type linear-to-circular polarization converter. *IEEE Trans Microw Theory Tech*, 68(10):4138-4149. https://doi.org/10.1109/TMTT.2020.3002248

Su T, Yi XJ, Wu B, 2019. X/Ku dual-band single-layer reflectarray antenna. *IEEE Antenn Wirel Propag Lett*, 18(2): 338-342. https://doi.org/10.1109/LAWP.2018.2890766

Tong XF, Jiang ZH, Li Y, et al., 2022. Dual-wideband dual-circularly-polarized shared-aperture reflectarrays with a single functional substrate for K-/Ka-band applications. *IEEE Trans Antenn Propag*, 70(7):5404-5417. https://doi.org/10.1109/TAP.2022.3145484

Wang DY, Liu FF, Liu T, et al., 2021. Efficient generation of complex vectorial optical fields with metasurfaces. *Light Sci Appl*, 10(1):67. https://doi.org/10.1038/s41377-021-00504-x

Wang YF, Ge YH, Chen ZH, et al., 2022. Broadband high-efficiency ultrathin metasurfaces with simultaneous independent control of transmission and reflection amplitudes and phases. *IEEE Trans Microw Theory Tech*, 70(1):254-263. https://doi.org/10.1109/TMTT.2021.3119376

Wu Q, Hirokawa J, Yin JX, et al., 2018. Millimeter-wave multibeam endfire dual-circularly polarized antenna array for 5G wireless applications. *IEEE Trans Antenn Propag*, 66(9):4930-4935. https://doi.org/10.1109/TAP.2018.2851667

Xu P, Li L, Li RJ, et al., 2021. Dual-circularly polarized spin-decoupled reflectarray with FSS-back for independent operating at Ku-/Ka-bands. *IEEE Trans Antenn Propag*, 69(10):7041-7046. https://doi.org/10.1109/TAP.2021.3076518

Zhang XL, Yang F, Xu SS, et al., 2021. Hybrid polarization-phase tuning methodology for reflectarray antennas. *IEEE Trans Antenn Propag*, 69(9):5534-5545. https://doi.org/10.1109/TAP.2021.3060023

Zhao Y, Luk KM, 2018. Dual circular-polarized SIW-fed high-gain scalable antenna array for 60 GHz applications. *IEEE Trans Antenn Propag*, 66(3):1288-1298. https://doi.org/10.1109/TAP.2018.2797530

Zhou M, Sørensen SB, Brand Y, et al., 2020. Doubly curved reflectarray for dual-band multiple spot beam communication satellites. *IEEE Trans Antenn Propag*, 68(3):2087-2096. https://doi.org/10.1109/TAP.2019.2950817